2023 IEEE International Conference on Robotics and Automation (ICRA 2023)
May 29 - June 2, 2023. London, UK

Fast, Reliable Constrained Manipulation Using a VSA Driven Planar Robot*

Andrew L. Bernhard[1] and Joseph M. Schimmels[2]

***Abstract*— This paper presents the design and performance of a planar 3R robot capable of dexterous constrained manipulation when interacting with a stiff environment. A novel variable stiffness actuator (VSA) having a stiffness ratio of approximately 500 is also described. Variable stiffness actuation, together with a combined position/compliance manipulation path, is used to: 1) allow the robot to passively comply with its environment along kinematically constrained directions despite model error in constraint locations, and 2) generate high stiffness for accurate motion control along kinematically unconstrained directions despite resisting forces. This manipulation strategy provides dexterity for cases in which mechanical work must be performed while complying with constraints. The manipulation strategy and robot performance were evaluated with the task of turning a steel crank to lift a weight. Results show that, when using passive compliance control, the robot completed the task 29 times faster with constraint forces 80% lower than when using traditional active compliance control (with VSAs at their highest stiffness).**

I. Introduction

Traditional industrial robot arms are designed for accurate absolute positioning in free space, necessitating high stiffness in the arm structure. When such a robot arm is required to interact with a stiff environment, any small position error associated with mechanical interference between the robot and the environment generates very large forces. These forces may damage the robot or the environment with which it is interacting.

One strategy to avoid large contact forces is to use some form of active force or impedance control [1]–[6]. Active control methods, however, have limitations with respect to stable interaction with stiff environments, especially at higher speeds [2], [7], [8].

Another strategy is to use conventional position control in conjunction with structured passive elastic behavior. Elastic behavior is characterized as stiffness or compliance, where compliance is the inverse of stiffness. The control law for this strategy at a given instant in time is given by

$$\mathbf{x} = \mathbf{x}_o + \mathbf{x}_c = \mathbf{x}_o + \mathbf{C}\,\mathbf{f} \tag{1}$$

where for particle planar cases $\mathbf{x} \in \mathbb{R}^2$ is the vector indicating the actual incremental position of the end-effector, $\mathbf{x}_o$ is the nominal (or commanded) incremental position of the end-effector (the increment for which the sequence of increments yields the path that would be successful in the absence of constraint model error), $\mathbf{x}_c$ is the position correction made by the robot in response to forces acting on it, $\mathbf{C} \in \mathbb{R}^{2x2}$ is the Cartesian compliance matrix, and $\mathbf{f} \in \mathbb{R}^2$ is the force acting on the end-effector.

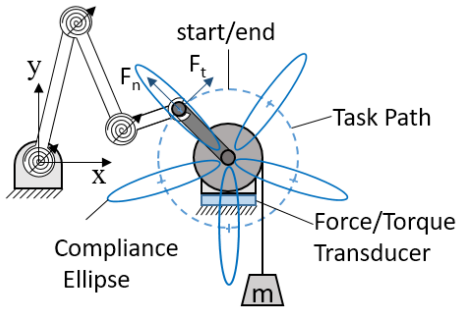

Fig. 1. Task Using Passive Compliance Control. While turning a crank to lift a weight, each VSA position and stiffness is modulated so that endpoint compliance yields stable force regulation and accurate relative positioning.

Dexterous manipulation is achieved using this strategy if the passive compliance is appropriately structured. Force regulation is attained if high compliance is used in constrained directions, and accurate commanded motions are attained if high stiffness is used in directions that are kinematically unconstrained. This manipulation strategy provides dexterity in any application requiring mechanical work to be performed (motion executed despite resisting forces) while also complying with kinematic constraints. Examples in kitchen assistance alone include cutting food and opening a door, a drawer, or a jar. Note that in most tasks, both the commanded position and commanded compliance appropriate for the task are time-varying.

Figure 1 illustrates a particularly difficult testbed constrained manipulation application in which a steel crank is turned to lift a weight. Here, using the passive compliance control approach, an end-effector path is executed and a task-appropriate passive compliance path is realized using a 3R manipulator with variable stiffness actuators (VSAs) at each joint. The series of ellipses in Fig. 1 indicate the task-appropriate endpoint compliance at different points of the manipulator end-effector trajectory. Throughout the task, high compliance along the crank handle axis minimizes constraint forces. In the direction that advances the crank, compliance is low so that the commanded motion is executed for successful task execution. (In the passive compliance

*This work was supported by the National Science Foundation under grant IIS-1427329.

[1]Andrew L. Bernhard is with X-Ray Science, Beamline Instrumentation, Argonne National Laboratory, Lemont, IL USA, abernhard@anl.gov

[2]Joseph M. Schimmels is with the Department of Mechanical Engineering, Marquette University, Milwaukee, WI, USA, j.schimmels@marquette.edu

control approach, the illustrated force/torque transducer is not used in motion correction; it is used only to measure interaction forces.)

To accomplish this task using passive compliance control, an appropriate trajectory in position and compliance is first defined in task space (i.e., the position/compliance trajectory, as illustrated in Fig. 1) and then tracked in the position/compliance joint space [9].

A significant amount of prior work has developed different VSA design strategies (summarized in [10]). Little work, however, has addressed the use of VSA-driven robots in performing kinematically constrained tasks. A limited amount of experimental benchmarking has shown that VSA-driven robots performing constrained manipulation are significantly faster and generate lower constraint forces than active force control. In [11], a passive compliance control approach was twice as fast with 80% less force than an active impedance control approach when performing a peg-in-hole assembly task.

With the passive compliance control strategy, *a priori* knowledge of the task is used to plan a path through the combined compliance/position task space. The realized robot Cartesian endpoint compliance is a function of each joint's individual compliance and the kinematic configuration of the arm, both of which are simultaneously controlled in real time throughout the task execution. The particle planar Cartesian endpoint compliance is calculated [12] as

$$\mathbf{C} = c_1 \mathbf{t}_1 \mathbf{t}_1^T + c_2 \mathbf{t}_2 \mathbf{t}_2^T + \cdots + c_n \mathbf{t}_n \mathbf{t}_n^T \tag{2}$$

where $c_i, i = 1, \ldots, n$ is the joint compliance for each of the n joints, and $\mathbf{t}_i$ is the joint twist determined by

$$\mathbf{t}_i = \pm\, \mathbf{\Omega} \mathbf{r}_i \tag{3}$$

where $\mathbf{r}_i \in \mathbb{R}^2$ is the position of joint i relative to the robot end-effector and $\mathbf{\Omega}$ is a 2×2 anti-symmetric matrix associated with a vector cross-product, given as:

$$\mathbf{\Omega} = \begin{bmatrix} 0 & 1 \\ -1 & 0 \end{bmatrix}. \tag{4}$$

The robot nominal path in position and compliance task space is designed assuming bounded error in task constraints. The position/compliance path is then executed without force feedback.

In this paper, the physical structure and the control system structure of the 3R VSA-driven robot built to evaluate the passive compliance control strategy are first described. Then, the design and performance of the novel VSA developed to achieve a very large selectable range in joint stiffness values are described. Next, the robot overall system performance is evaluated experimentally in a highly constrained manipulation task (turning a crank to lift a weight) for 2 cases, one using passive compliance control and the other using active compliance control. A brief summary is then presented.

II. VSA-Driven 3R Robot Description

The 3R planar robot arm using variable stiffness actuation shown in Fig. 2 was designed and fabricated. The global coordinate system used for the manipulator is fixed at the center of the first joint. The first joint angle θ_1 is defined relative to the positive x axis. Joint angles θ_2 and θ_3 are each defined relative to the angle of their respective preceding link. Each VSA joint has a motor to actuate the stiffness selection mechanism and a motor to control the joint position.

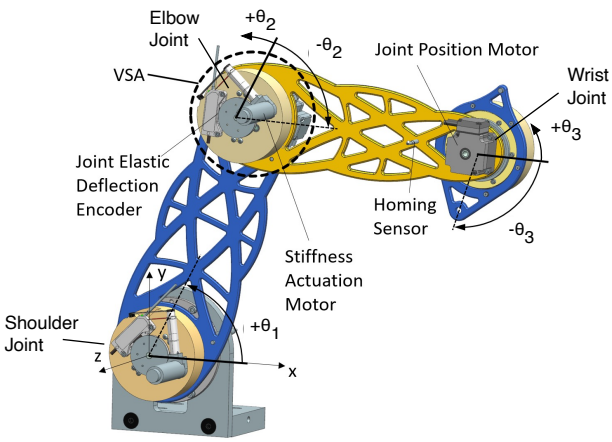

Fig. 2. CAD Assembly Drawing of VSA-Driven 3R Robot.

TABLE I
Robot Physical Parameters

Parameter	Units	Link 1	Link 2	Link 3
Length	m	0.32	0.30	0.08
Mass	kg	0.448	0.376	0.0898
COM Distance	m	0.156	0.136	0.0067

A. Robot Physical Structure

Robot link lengths, masses, and distances to the center of mass (COM) from the more-proximal joint center are listed in Table I. The robot links are numbered from proximal to distal (1-3). Each link has a large amount of interior void space to be lightweight and very stiff. High stiffness is needed to ensure that the elastic behavior of the VSA dominates the compliance of the link/joint system even when the joint is set to its highest stiffness. The robot arm is designed to accurately position a load of 6 kg when each joint is set at its maximum stiffness and the arm is fully outstretched horizontally.

Finite element analysis was performed using NX Nastran on each link as part of geometry refinement to ensure low weight and high stiffness. Results of the analysis of the first link (Fig. 3) show that the maximum deflection associated with the rated load is 0.080mm, whereas the shoulder joint flexure under the same load will result in a deflection of 0.167mm at the distal end of Link 1 when set at its highest stiffness setting. When at its maximum stiffness, each VSA has at least twice the compliance of its adjacent links.

At lower joint stiffness settings, more deflection from equilibrium can be accommodated, but the load rating is decreased. The limiting factor in load accommodation is the stress in the VSA joint flexure (FEM analysis described in

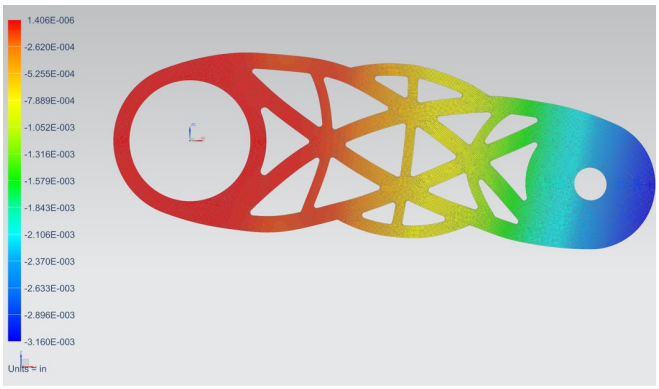

Fig. 3. FEA Calculated Deflection of Link 1 Under Maximum Load.

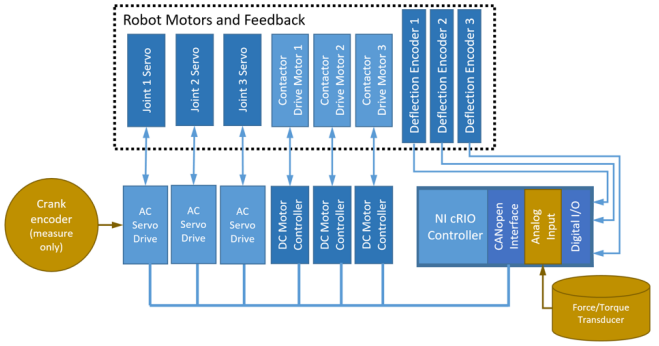

Fig. 4. Robot Control and Instrumentation. Robot control architecture is shown in blue. Additional instrumentation is shown in gold.

Sec. III). Each joint was designed to accommodate 13mm of deflection at the end effector without plastic deformation when the arm is fully outstretched.

B. Robot Control Structure

Robot position and compliance are controlled by a LabVIEW Virtual Instrument (VI) running on a National Instruments compactRIO-9064 (cRIO). This controller is capable of executing pre-programmed motion and compliance profiles by commanding synchronous motion of the motors. Two modules were installed in the cRIO: 1) a digital I/O module for reading joint deflection encoders, and 2) a CAN module for bidirectional communication with the motor drives using the fast CANopen industrial communication protocol. The CANopen protocol is capable of communication speeds of 1 Mbit/s.

Fig. 4 illustrates the structure of the robot control/instrumentation system. Each motor drive sends and receives information directly to/from the cRIO. The drives are uniquely addressed and connected in parallel, enabling synchronous motion.

Each joint has a harmonic drive actuator for link positioning. The motor in each is a three phase permanent magnet AC servomotor. Each motor is controlled by a Kollmorgen AKD AC servo drive. While many AC servo drives are commercially available to control such motors,

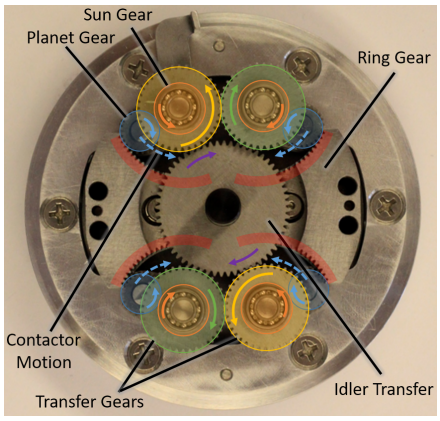

Fig. 5. Transmission Driving the 4 Contactors along the Flexure's 4 Beams.

this model was chosen due to its compatibility with the CANopen protocol and the flexibility of using additional encoder inputs. Each motor has an incremental encoder to close a position feedback loop with its respective drive. A homing routine for each joint using an inductive proximity sensor is used to set the zero position.

Each joint also has a Maxon DC gearmotor for joint stiffness modulation. Like the AC servo drives, the Maxon DC motor control boards use the CANopen protocol. With all 6 drives on the same network, motion in position and compliance actuator space can be synchronously commanded. Each stiffness modulation motor is equipped with an incremental encoder for position feedback and is homed with an inductive proximity sensor. Joint flexure deflection from equilibrium is measured directly with a 19-bit absolute encoder yielding a resolution of 6.87e-4 degrees (12.0 µrad). A digital I/O module in the cRIO is interfaced to the absolute encoders through RS-485 transceiver modules. The encoders communicate using the BISS-C serial protocol. For the cRIO to read data from the encoders, a VI uses the cRIO's FPGA to send clock pulses to the encoders and receive the data sent from the encoders. If the flexure deflection limit is exceeded, a fault is triggered and robot motion is stopped.

III. Multi-Beam Variable Stiffness Actuator

Each joint of the designed robot is powered by a novel VSA [13] consisting of a harmonic drive actuator attached to link *i* that controls joint angular position and a DC motor attached to link *i+1* that controls joint stiffness. The DC motor drives a transmission that converts the stiffness motor angular position to the angular position of levers that connect to four parallel axes offset from the joint center. Each lever (contactor) rolls along one beam of a 4-beam flexure.

A single stiffness actuator in each joint drives each of the 4 contactors to the same relative position along a flexure beam using a stiff, low friction transmission. To attain low friction, each contactor rolls along the flexure using a needle bearing and ball bearings are used throughout the design . Each contactor (lever) moves with the carrier arm of a planetary gear system which gives the transmission very

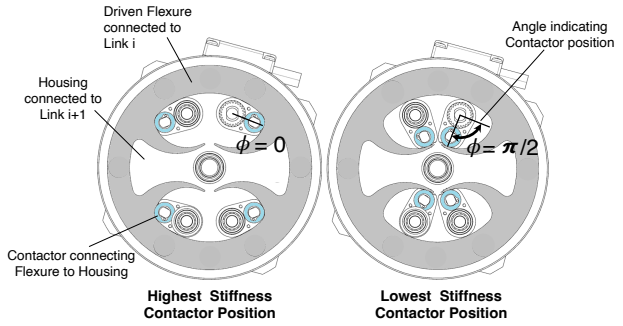

Fig. 6. Joint Stiffness Determined by Contactor Angle, ϕ. Stiffness decreases exponentially from its highest value when $\phi = 0$ to its lowest value when $\phi = \pi/2$.

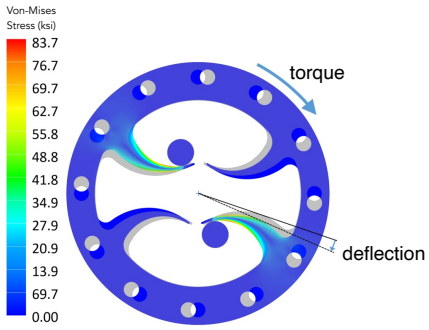

Fig. 7. FEA Evaluation of Flexure Load-Deflection Relationship. Flexure unloaded state position is shown in gray and its deflected position and stresses are shown in color.

high stiffness. Fig. 5 illustrates the planetary gear system that generates the appropriate concurrent motion of the 4 contactors. Each contactor needle bearing is concentric with a planet gear (blue gears in Fig. 5) of a distinct planetary gear system. The rings of each of these planetary gear systems are machined in a two-piece component which has a half above and a half below the flexure element. Each sun gear (orange) of the four planetary gear systems are driven synchronously. The sun gears are connected to outer transfer gears (yellow and green) that mesh in adjacent pairs. The yellow gears are connected by a central idler gear. The idler gear is in a separate plane from the green gears and meshes only with the yellow gears which are thicker and mesh on a lower plane.

The 4-beam flexure and contactors are illustrated in Fig. 6. The variation in stiffness relates to the elastic properties of the 4 cantilever beams. Each beam has very high stiffness when contacted at its base and exhibits low stiffness when contacted at its tip. The flexure beams are designed such that stiffness varies continuously from high to low in an exponential relationship with the contactor angle position (ϕ in Fig. 6). The exponential relationship yields constant relative sensitivity ($\delta k/\delta\phi = \lambda k$), where λ is a constant. The exponential relationship selected is given by

$$k = k_o e^{-\lambda\phi}, \quad (0 \leq \phi \leq \pi/2) \tag{5}$$

where k is the torsional stiffness of the joint, k_o is the maximum stiffness value for the joint, and ϕ is the angle that indicates where along the beam contact occurs. If the value of λ exceeds 4.4, then the ratio of highest to lowest stiffness is greater than 1000. The constants k_o and λ are determined by the flexure material and the beam geometry.

As seen in Fig. 6, the flexure consists of 4 tapered curved cantilever beams supported at the joint periphery by the harmonic drive transmission. The curve on one side of a flexure beam coincides with the arc traced by the contactor tip as it moves through its range of motion. The side of the beam opposite the contactor is defined by a single arc terminating as a straight section at the beam tip. The flexure material and the geometry of that arc determine the relationship between joint stiffness and contactor angle.

The 3 VSA joints of the robot are the same except

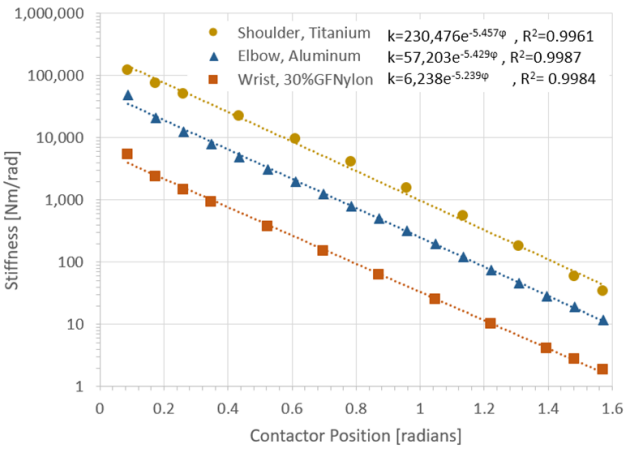

Fig. 8. FEA Calculated Flexure Stiffness Variation with Contactor Angle. The different material and geometry of each of the 3 flexures yields joint location appropriate elastic behavior.

for the flexure material and flexure beam geometry. The flexure material and arc geometry for each were determined using finite element analysis in NX Nastran. An iterative process of adjusting both the arc radius and the arc center location and then evaluating the corresponding FEA results was performed until a geometry was found that gave the desired exponential relationship between joint stiffness and contactor location (5) with a value of the exponent constant $\lambda > 4.4$.

To perform the analysis, the flexure geometric model was simplified to 2D plate type elements. The analysis for each flexure was run for a minimum of 11 points along the full range of contactor angles. For each contactor angle, contact at the flexure was modeled as a fixed boundary condition. The outer circumference was also constrained to only allow rotation about the flexure geometric center (the joint axis). A torque was applied to the outer circumference of the flexure. The maximum stress in the flexure was evaluated to ensure that expected loads do not exceed material elastic limits. Fig. 7 illustrates flexure loading, the calculated flexure deflection, and local stresses on the flexure. The average

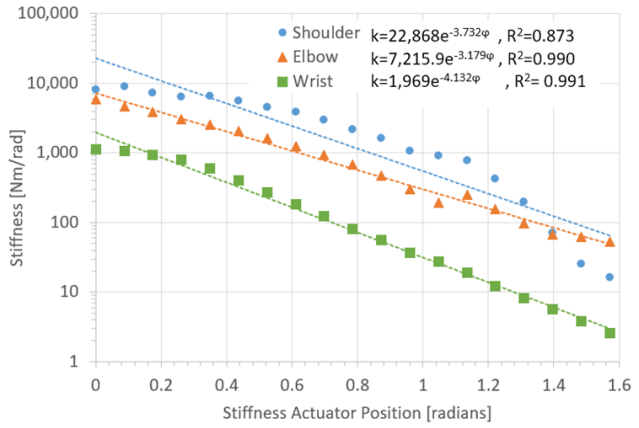

Fig. 9. Experimental Joint Stiffness Variation with Contactor Angle.

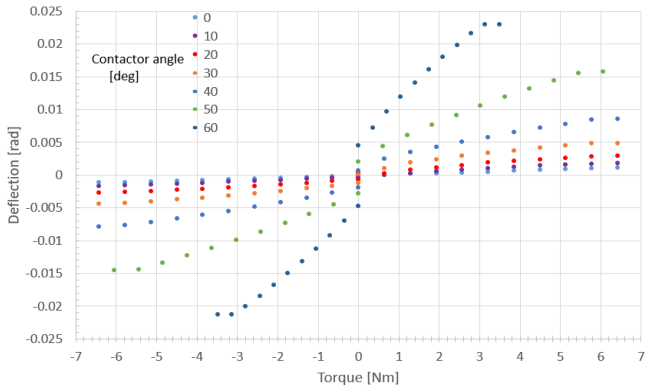

Fig. 10. Elbow Deflection-Torque Relationship for Different Contactor Angles.

nodal displacement of the flexure outer circumference was recorded and used to calculate the angular displacement of the loaded flexure. The FEA calculated relationship between stiffness and contactor angle for each of the 3 flexures is summarized in Fig. 8.

Each of these 3 flexures was fabricated and incorporated into a VSA which was then tested to obtain the joint overall stiffness variation with contactor angular position. The experimental results for each VSA are summarized in Fig. 9. As expected, results show that the overall joint stiffness is less than the numerically calculated stiffness of the flexure itself.

The experimentally obtained relationship between joint deflection and applied torque is very close to linear for each of the 3 VSAs. Fig. 10 illustrates this relationship for multiple contactor angles for the elbow joint. Note that, except for the lowest torque values at the lower stiffness settings, the behavior is very close to linear. The offset from zero deflection for the low stiffness settings is likely due to some backlash in the contactor-flexure relative positioning near the beam tip.

Important VSA performance criteria (identified in [14]) for each joint are summarized in Table II.

TABLE II
VSA PERFORMANCE CRITERIA

Performance Criterion	Units	Shoulder	Elbow	Wrist
Full Stiffness Variation Time	ms	200	200	200
Maximum Stiffness	Nm/rad	8120	5830	1120
Maximum Deflection	deg	0.45	0.28	0.25
Minimum Stiffness	Nm/rad	16.5	53.2	2.61
Maximum Deflection	deg	1.3	2.6	9.1
Maximum Torque	Nm	64	28	4.8
Weight	kg	1.0	1.0	1.0
Weight (including actuator)	kg	3.5	2.2	1.4

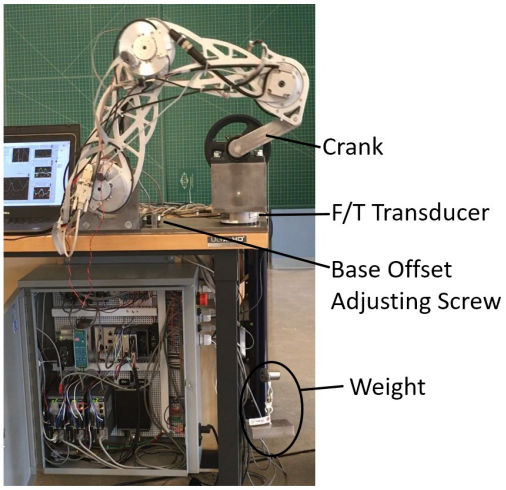

Fig. 11. VSA-Driven Robot Test Appartatus.

IV. VSA-DRIVEN 3R ROBOT PERFORMANCE

The robot ability to perform constrained manipulation was tested with a physical task of turning a crank to lift a 19.6N weight. A photo of the robot and crank system is shown in Fig. 11. This task is particularly challenging because the desired end-effector motion is bilaterally constrained by a very stiff environment along a single degree of freedom, along which a force resisting task progress is imposed. The manipulator must generate a force sufficient to lift a weight while minimizing forces normal to the crank path. Because the crank pulley radius was 6.35cm and the crank length was 14cm, the effective load resisting path progress was approximately 9N. In addition, to demonstrate approach robustness, an intentional error (a 1.59mm crank center offset) in the task constraint model was imposed. The compliance control law (1) was realized both passively and actively and the results compared.

In the passive compliance realization approach, the desired compliant behavior was implemented by controlling both the joint position and joint stiffness. The joint paths for each are illustrated in Figs. 12 and 13. In the direction tangent to the path, the end-effector stiffness was 6 times greater than its stiffness normal to the path. The time to turn the crank one full revolution was 6.1s. Faster times were not attempted to prevent inertial forces from causing plastic deformation of the VSA flexures.

In the active compliance realization approach, the com-

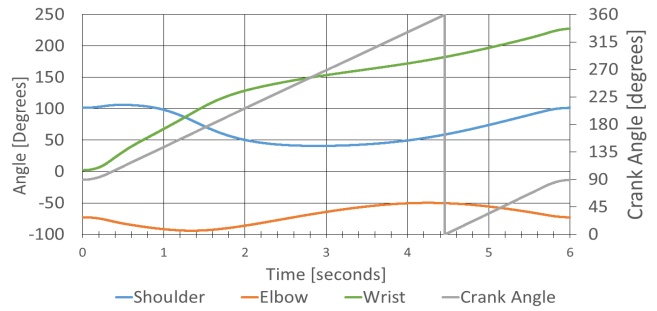

Fig. 12. Commanded Joint Position Variation in Time.

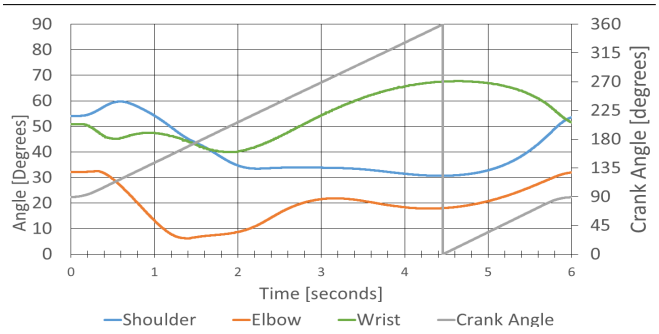

Fig. 13. Commanded Joint Compliance Motor Position Variation in Time.

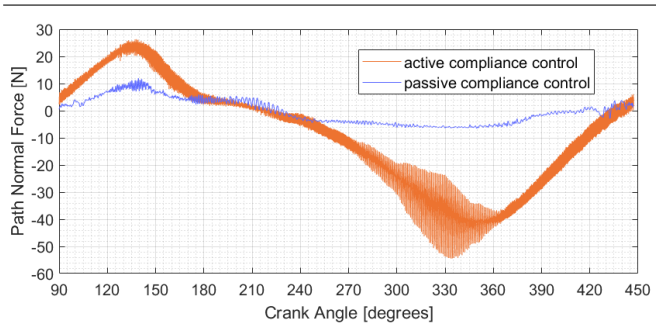

Fig. 14. Path Normal Force Variation with Crank Angle.

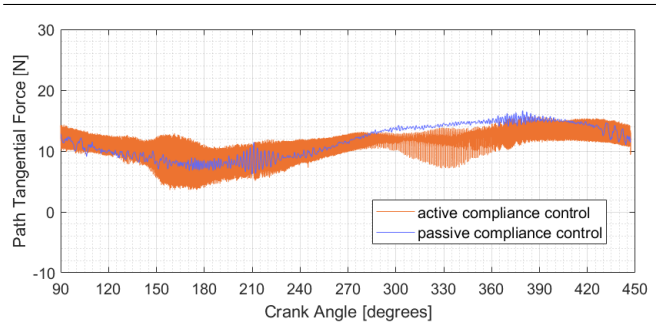

Fig. 15. Path Tangential Force Variation with Crank Angle.

manded motion path consists of a sequence of 1 mm incremental steps in position. The motor feedback gains (the values in a diagonal compliance matrix) were tuned for the system (the robot/crank combination) so that position step sizes do not lead to excessive constraint forces or instability. In each step, a 36Hz ringing in the force signal (induced by robot motion) was observed. To reduce noise in the force signal so that a better indication of actual constraint forces is obtained, a relatively smooth incremental motion was commanded (inducing less vibration) and a wait time was used to filter the force signals before the next motion was commanded. A trapezoidal velocity profile was used for each motion, with 100ms to complete the motion followed by a pause for 100ms (approximately 4 oscillation periods) to measure and average the forces. The averaged force was then scaled by the compliance matrix to determine the appropriate corrective motion ($\mathbf{x_c}$ in (1)) which is added to the next nominal motion step. The time to turn the crank one full revolution was 175.4s. Therefore, the passive compliance control method was approximately 29 times faster than the active compliance force feedback method.

Fig. 14 shows forces normal to the path and Fig. 15 shows forces tangent to the path as the crank is turned for both the passive and active implementations of compliance control. Indicated forces were sampled at 2ms intervals and smoothed using a 100ms running average. The active compliance control force signals were very noisy despite the filtering performed. The measured average tangential force was consistent with the applied load of 9N with a peak-to-peak variation of about 8N for both the passive and active approach. In the normal direction, the peak-to-peak force variation observed while turning the crank with the passive method is approximately 15N; whereas, the peak-to-peak force variation for the active control method is approximately 80 N. Therefore, the passive implementation yielded a 80% reduction in constraint forces.

V. Summary

The passive compliance control approach provides dexterous manipulation in tasks that would not even be attempted using traditional position control. Experimental results show that the passive compliance control approach yields both stable interaction with kinematic constraints and the ability to simultaneously perform mechanical work in directions that are not kinematically constrained. A comparison of experimental results for the task of turning a stiff crank to lift a weight shows that the passive compliance control approach was almost thirty times faster than when using active force control with less than a fifth of the constraint forces.

References

[1] N. Hogan, "Impedance control: An approach to manipulation," *ASME Journal of Dynamic Systems, Measurements, and Control*, vol. 107, no. 3, 1985.

[2] W. S. Newman, "Stability and performance limits of interaction controllers," *ASME Journal of Dynamic Systems, Measurements, and Control*, vol. 114, no. 4, pp. 563–570, 1992.

[3] E. Fasse and J. Broenink, "A spatial impedance controller for robotic manipulation," *IEEE Transactions on Robotics and Automation*, vol. 13, no. 4, pp. 546–556, 1997.

[4] F. Caccavale, C. Natale, B. Siciliano, and L. Villani, "Six-dof impedance control based on angle/axis representations," *IEEE Transactions on Robotics and Automation*, vol. 15, no. 2, 1999.

[5] A. Albu-Schaffer, C. Ott, and G. Hirzinger, "A unified passivity-based control framework for position, torque, and impedance control of flexible joint robots," *International Journal of Robotics Research*, vol. 26, no. 1, 2007.
[6] F. Caccavale, C. Natale, B. Siciliano, and L. Villani, "Integration for the next generation: Embedding force control into industrial robots," *IEEE Robotics and Automation Magazine*, vol. 12, no. 3, 2005.
[7] N. Hogan, "On the stability of manipulators performing contact tasks," *IEEE Journal of Robotics and Automation*, vol. 4, no. 6, December 1988.
[8] C. Yang, G. Ganesh, S. Haddadin, S. Parusel, A. Albu-Schaffer, and E. Burdet, "Human-like adaptation of force and impedance in stable and unstable interactions," *IEEE Transactions on Robotics*, vol. 27, no. 5, October 2011.
[9] J. J. Rice and J. M. Schimmels, "Passive compliance control of redundant serial manipulators," *ASME Journal of Mechanisms and Robotics*, vol. 10, no. 4, August 2018.
[10] R. V. Ham, T. G. Sugar, B. Vanderborght, K. W. Hollander, and D. Lefeber, "Compliant actuator designs: Review of actuators with passive adjustable compliance/controllable stiffness for robotic applications," *IEEE Robotics and Automation Magazine*, vol. 16, no. 3, 2009.
[11] B.-S. Kim, Y.-L. Kim, and J. Song, "Preliminary experiments on robotic assembly using a hybrid-type variable stiffness actuator," in *Proceedings of the 2011 IEEE/ASME International Conference on Advanced Intelligent Mechatronics*, 2011.
[12] S. Huang and J. M. Schimmels, "Synthesis of point planar elastic behaviors using 3-joint serial mechanisms of specified construction," *ASME Journal of Mechanisms and Robotics*, vol. 9, pp. 011 005(1–11), February 2017.
[13] J. M. Schimmels, A. Bernhard, and J. Rice, "Variable stiffness serial elastic actuator," *U. S. Patent*, no. 11,192,266.
[14] G. Grioli, S. Wolf, M. Garabini, M. Catalano, E. Burdet, D. Caldwell, M. Catalano, W. Freidl, M. Grebenstein, M. Laffranchi, D. Lefeber, S. Stramigioli, N. Tsagarakis, M. V. Damme, B. Vanderborght, A. Albu-Schaffer, and A. Bicchi, "Variable stiffness actuators: The user's point of view," *International Journal of Robotics Research*, 2015.